Combustion and Flame 158 (2011) 860–875

Contents lists available at ScienceDirect

Combustion and Flame

journal homepage: www.elsevier.com/locate/combustflame

Effects of gravity and pressure on laminar coflow methane–air diffusion flames at pressures from 1 to 60 atmospheres

Marc R.J. Charest *, Clinton P.T. Groth, Ömer L. Gülder

University of Toronto, Institute for Aerospace Studies, 4925 Dufferin Street, Toronto, Ontario, Canada M3H 5T6

ARTICLE INFO

Article history:
Received 12 October 2010
Received in revised form 20 January 2011
Accepted 20 January 2011
Available online 12 February 2011

Keywords:
High pressure combustion
Zero-gravity combustion
Diffusion flames
Soot modeling

ABSTRACT

The effects of pressure and gravity on the sooting characteristics and flame structure of coflow methane–air laminar diffusion flames between 1 and 60 atm were studied numerically. Computations were performed by solving the unmodified and fully-coupled equations governing reactive, compressible flows which include complex chemistry, detailed radiation heat transfer and soot formation/oxidation. Soot formation/oxidation was modeled using an acetylene-based, semi-empirical model which was verified with previously published experimental data to correctly capture many of the observed trends at normal-gravity. Calculations for each pressure considered were performed under both normal- and zero-gravity conditions to help separate and identify the effects of pressure and buoyancy on soot formation. Based on the numerical predictions, pressure and gravity were observed to significantly influence the sooting behavior and structure of the flames through their effects on buoyancy and temperature. Zero-gravity flames generally have lower temperatures, broader soot-containing zones, and higher soot volume fractions than normal-gravity flames at the same pressure. Buoyancy forces caused the normal-gravity flames to narrow with increasing pressure while the increased soot concentrations and radiation at high pressures caused the zero-gravity flames to lengthen. Low-pressure flames at both gravity levels exhibited a similar power-law dependence of the maximum carbon conversion on pressure that weakened as pressure was increased. In the zero-gravity flames, increasing pressure beyond 20 atm caused the maximum carbon conversion factor to decrease.

1. Introduction

Fully understanding the behavior of diffusion flames is critical to the development of high-efficiency, pollutant-free combustion devices and fire-suppression systems for space applications. Two key areas of interest which are not well-characterized due to their complex nature are the physics and chemistry related to soot formation. Soot is a harmful pollutant that negatively affects the performance of practical combustion devices, which typically operate at elevated pressures, and greatly influences the spread of flames in space. However, our current understanding of the effects of pressure and gravity on soot formation/oxidation is limited since previous experimental and numerical studies generally focused on normal-gravity atmospheric flames [1–11]. This study aims to characterize these effects through the numerical analysis of laminar diffusion flames at pressures ranging from 1 to 60 atm and various levels of gravity. Even though most practical flames are turbulent, these results for laminar flames can be applied to turbulent flames through various modeling approaches such as the laminar flamelet concept [12].

Both pressure and gravity profoundly influence the structure and sooting characteristics of laminar diffusion flames [13,14]. This influence occurs through the effects of pressure and gravity on buoyant forces which rapidly accelerate the expanding hot gases. Since the effective gravitational acceleration scales with pressure-squared, increasing pressure drastically alters the shapes of normal-gravity flames. For example, increasing pressure in laminar diffusion flames causes flow streamlines to contract towards the centerline and the flame diameter to decrease [15–18]. Miller and Maahs [15] suggested that this change in flame diameter with pressure is likely due to changes in chemistry. Experimental measurements [17–20] and numerical predictions [21] for soot volume fraction indicate that the flame diameter is proportional to $p^{-1/2}$. These findings imply that residence time is independent of pressure for constant fuel mass flow rates since the cross-sectional area of the flame varies inversely with pressure. This was confirmed numerically by Liu et al. [21] who showed that the axial velocity along the flame centerline was roughly independent of pressure. If residence time does not change with pressure, flame height should also remain constant. Roper's correlations for buoyancy-dominated laminar jet diffusion flames [22,23] state that the

* Corresponding author.
E-mail address: charest@utias.utoronto.ca (M.R.J. Charest).

0010-2180/$ - see front matter © 2011 The Combustion Institute. Published by Elsevier Inc. All rights reserved.
doi:10.1016/j.combustflame.2011.01.019

visible flame height, to a first-order approximation, is independent of pressure and depends on mass flow rate only. However, Miller and Maahs [15], Flower and Bowman [16], McCrain and Roberts [17], and Thomson et al. [18] have all observed pressure-dependent flame heights in experiments involving high-pressure laminar diffusion flames. These experiments showed that the visible flame height generally increased with pressure at low pressures, remained constant over a range of pressures, and then decreased with further increase in pressure. Recently, Bento et al. [19] and Joo and Gülder [20] observed pressure-independent visible flame heights over a wide range of pressures. Constant flame heights were also predicted numerically by Liu et al. [21] and Charest et al. [24].

As pressure is increased in normal-gravity flames, measured soot volume fractions increase since the flame narrows and soot must flow through a smaller cross-section. This narrowing of the flame causes local temperatures near the centerline to increase and fuel pyrolysis rates in the central core to intensify. Enhanced air entrainment into the flame near the burner is also expected to increase pyrolysis rates [21]. Miller and Maahs [15] estimated total soot concentrations in high-pressure axisymmetric methane–air diffusion flames between 1 and 50 atm from measurements of the flame emissive power. The data indicates that soot yield is proportional to p^n, where n is approximately 1.7 ± 0.7 up to 10 atm. Above 10 atm, the dependence of soot yield on pressure decreased significantly. Flower and Bowman [16] studied laminar diffusion flames of ethylene at pressures between 1 and 10 atm by measuring line-of-sight integrated soot volume fractions and temperatures along the flame centerline. They reported maximum diameter-integrated soot volume fractions proportional to $p^{1.2}$. Measurements made by Lee and Na [25] in laminar ethylene diffusion flames from 1 to 4 atm indicated a $p^{1.26}$ dependence of the maximum diameter-integrated soot volume fraction on pressure. McCrain and Roberts [17] obtained similar pressure exponents in methane flames from 1 to 25 atm and ethylene flames from 1 to 16 atm based on path-integrated and local soot volume fraction measurements. Radially-resolved soot concentration and temperature measurements were reported by Thomson et al. [18] for methane diffusion flames from 5 to 40 atm. These measurements were later extended to 60 atm by Joo and Gülder [20]. Both concluded that the maximum amount of fuel carbon converted to soot, which is most suitable for assessing the sensitivity of soot formation to pressure [16], varied proportional to p between 5 and 20 atm. Between 30 and 60 atm, Joo and Gülder measured a pressure exponent equal to 0.33. Similar soot and temperature measurements were made by Bento et al. [19] for propane flames from 1 to 7.2 atm.

Non-buoyant flames are both longer and wider than their buoyant counterparts [26–28]. Non-buoyant flames are wider because there is no upward acceleration to induce an inward radial motion that would cause the flame to contract. However, the reason for the lengthening of flames when buoyancy is eliminated is not clear. Investigators have cited causes such as the increased importance of axial diffusion [29,30], the lack of radial convection [31], reduced mass diffusivities associated with lower flame temperatures [28], and reduced flame temperatures in general [32]. Roper's model for circular port burners, which includes radial convection and neglects axial diffusion, states that flame length should be independent of gravity [22].

Soot particles are too large to be transported like gas molecules (i.e., via molecular diffusion) and are instead convected by the gas flow. Therefore, the path and residence time of soot particles in laminar diffusion flames are strongly affected by buoyancy since buoyant forces drastically alter the flow field [33]. For example, the dividing streamline, which originates from the edge of the burner, diverges radially-outward in non-buoyant jet diffusion flames and converges towards the centerline in buoyant ones [34]. Residence times for particles in non-buoyant flames are much longer than for particles in buoyant flames since local gas flow velocities are lower. These effects of buoyancy on the gas flow field and particle path cause non-buoyant diffusion flames to exhibit broader soot-containing regions and larger soot oxidation regions [27]. Higher soot concentrations and bigger particles are also observed in non-buoyant flames as a result [35–37].

Although there are many experimental studies on the sooting characteristics of non-buoyant diffusion flames, none specifically address the combined effects of pressure and gravity on flame structure. Smoke-point measurements reported by Sunderland et al. [33] and Urban et al. [38] for flames between 0.3 and 2 atm with various gaseous hydrocarbon fuels indicated that the laminar smoke-point flame lengths of non-buoyant flames were much shorter than equivalent buoyant flames. Ku et al. [36] measured soot particle sizes in laminar diffusion flames of propane and ethylene under normal- and micro-gravity conditions. They found that primary particle sizes were larger in non-buoyant flames due to the longer residence times. Soot volume fractions were measured and soot particles sampled in weakly-buoyant gaseous laminar diffusion flames at sub-atmospheric pressures by Sunderland et al. [39–41]. These authors exploited the fact that the buoyancy-induced acceleration scales with p^2g, where g is the gravitational acceleration. However, Panek and Gülder [42] recently found that low-pressure experiments are not representative of true, zero-gravity conditions as flames are not completely isolated from the effects of gravity and reactions rates are slow. Measured soot volume fractions follow trends similar to those observed in high-pressure flames instead. Others have obtained quantitative two-dimensional measurements for soot volume fraction in either reduced-gravity [35,37,43–45] or zero-gravity [34,46,47] environments. Generally, measured peak soot concentrations in micro-gravity flames are approximately a factor of two larger than those measured in normal-gravity flames. None of these studies considered pressures beyond one atmosphere.

Numerical modeling is an attractive tool to study the effect of pressure and gravity on soot formation in gaseous laminar diffusion flames. Measurements in high-pressure laminar diffusion flames are complicated by small flame diameters and limited optical access [21] while it is difficult and costly to conduct zero-gravity experiments [13]. However, there are only a few numerical studies of the effects of gravity [27,48–51] and pressure [21,52] on soot formation in gaseous laminar diffusion flames. Furthermore, none of these studies have looked at the effects of pressure in the absence of gravity.

Various approaches for modeling soot in laminar coflow diffusion flames have been successfully applied [53]. Soot models consist of two main components: a mathematical representation of the aerosol dynamics and a kinetic mechanism to describe gas-particle conversion. To model aerosol dynamics, researchers have either assumed a mono-disperse particle size distribution (PSD) [21,54–56], called the two-equation model, or applied more advanced moment [57–60] or sectional [7,61–63] representations. Sectional models are generally regarded as the most accurate, although they are computationally demanding, while moment models seem to provide the best balance between cost and accuracy [64]. The two-equation model is the simplest, making it suitable for large parametric studies.

Soot models applied in early studies of laminar diffusion flames typically employed semi-empirical chemistry sub-models which based the formation and growth of soot on one or two gaseous precursor species, such as acetylene [54,55] or benzene [65]. These models use simple global reaction mechanisms to describe the rates of the key processes such as nucleation, growth, and oxidation. Detailed sub-models incorporate more physical features like combination reactions between large polycyclic aromatic

hydrocarbons (PAH) and surface growth through the hydrogen-abstraction-acetylene-addition (HACA) mechanism [7,58,66]. These types of mechanisms require considerably more computational effort since detailed gas-phase chemical kinetics are required to describe the formation of large carbon ring structures. It is not completely clear whether the added computational expense is warranted, although some numerical studies have shown that certain phenomena—soot suppression via hydrogen addition, for example—are not accounted for in simple acetylene-based soot models [56]. Mehta et al. [11] concluded that computed soot volume fractions were rather insensitive to choice of nucleation model (acetylene- or PAH-based).

The goal of the present work is to numerically study the effects of buoyancy and pressure on the structure of laminar diffusion flames. As a starting point, the high-pressure methane–air flames studied by Joo and Gülder [20] are modeled and the predictive accuracy of the numerical model assessed. The numerical results were also used to explain some of the experimental observations. A second set of calculations were performed neglecting gravity in an attempt to separate the effects of buoyancy and pressure on soot formation. This paper first presents a brief overview of the numerical model and the coflow burner configuration. Following this overview, the current results are discussed and the conclusions presented.

2. Numerical model

The present study makes use of a previously developed framework for modeling laminar reactive flows with complex chemistry, non-gray radiative heat transfer and soot [67]. This framework mathematically describes the gaseous combusting flow using the conservation equations for continuous, multi-component compressible gas mixtures [68]. The equations consist of the conservation of total mass, individual species mass, mixture momentum, and mixture energy. Soot formation and destruction is modeled using an approach similar to those developed by Leung et al. [54] and Fairweather et al. [55]. In this approach, the soot particle size distribution is approximated by an average size that varies via surface reactions and coagulation. The representation requires only two additional transport equations for soot mass and number, which are given by

$$\frac{\partial}{\partial t}(\rho Y_s) + \nabla \cdot [\rho Y_s(\mathbf{v} + \mathbf{V}_Y)] = S_Y \tag{1}$$

$$\frac{\partial}{\partial t}(\rho N_s) + \nabla \cdot [\rho N_s(\mathbf{v} + \mathbf{V}_N)] = S_N \tag{2}$$

where t is the time, ρ is the mixture density, $\mathbf{v}$ is the mixture velocity vector, Y_s is the mass fraction of soot, N_s is the soot number density (number of particles per unit mass of mixture), $\mathbf{V}_Y$ is the diffusion velocity related to soot mass, $\mathbf{V}_N$ is the diffusion velocity related to soot number, S_Y is the time rate of change of the soot mass, and S_N is the time rate of change of the soot number. The time rate of change of gaseous species includes contributions from both gas-phase chemistry and soot surface reactions. The density of the mixture was calculated using the following state equation:

$$\rho = \frac{p}{R_u T\left(\sum_{k=1}^{N} Y_k / M_k\right)} \tag{3}$$

where p is the mixture pressure, Y_k is the mass fraction of the kth gaseous species, N is the number of gaseous species in the mixture, R_u is the universal gas constant, T is the temperature, and M_k is the species molar mass.

Multi-species diffusion was modeled here using the first-order Hirschfelder and Curtiss approximation [69] while soot was assumed to diffuse primarily by thermophoresis using an empirical model valid for all Knudsen numbers [70]. In addition to contributions from thermophoresis, a small Fickian diffusive flux was included in the soot particle transport equations. This was required to enhance numerical stability even though the transport of soot via Brownian motion is generally negligible. A similar procedure was taken by Kennedy et al. [71]. The resulting diffusion velocities for soot are

$$\mathbf{V}_Y = -\frac{D_s}{Y_s}\nabla Y_s + \mathbf{V}_T \tag{4}$$

$$\mathbf{V}_N = -\frac{D_s}{N_s}\nabla N_s + \mathbf{V}_T \tag{5}$$

where $D_s = 10^{-8}\ \mathrm{m^2/s}$ is the soot diffusion coefficient. Similarly, Kennedy et al. [71] specified a value for D_s equal to 1% of the gas diffusivity. The thermophoretic velocity, $\mathbf{V}_T$, for the soot particles is [70]

$$\mathbf{V}_T = -C_t \frac{\mu}{\rho T}\nabla T \tag{6}$$

where μ is the mixture dynamic viscosity and C_t is a numerical factor of order unity computed using an interpolation formula. In the free-molecular regime, $C_t = 0.55$ [72].

2.1. Soot chemistry model

Soot formation and destruction was modeled using the simplified soot kinetics described by Liu et al. [21,73]. This model is based on the reduced soot mechanisms of Leung et al. [54] and Fairweather et al. [55] which describe the evolution of soot through four basic steps—nucleation, surface growth, coagulation, and oxidation. Acetylene is assumed to be the only precursor responsible for the presence of soot. The resulting mechanism is

$$C_2H_2 \rightarrow 2C(s) + H_2 \tag{R1}$$

$$C_2H_2 + n \cdot C(s) \rightarrow (n+2) \cdot C(s) + H_2 \tag{R2}$$

$$C(s) + \frac{1}{2}O_2 \rightarrow CO \tag{R3}$$

$$C(s) + OH \rightarrow CO + H \tag{R4}$$

$$C(s) + O \rightarrow CO \tag{R5}$$

$$n \cdot C(s) \rightarrow C_n(s) \tag{R6}$$

It follows from the mechanism above that the source term in (1) can be written as

$$S_Y = 2M_s(R_1 + R_2) - (R_3 + R_4 + R_5)A_s \tag{7}$$

where M_s is the molar mass of soot (assumed equal to the molar mass of carbon, 12 kmol/kg) and A_s is the surface area of soot per unit volume of aerosol. The terms R_3, R_4, and R_5 are the soot oxidation rates for reactions involving O_2, OH, and O, respectively. The terms R_1 and R_2 are the soot nucleation and surface growth rates defined by

$$R_1 = k_1[C_2H_2] \tag{8}$$

$$R_2 = k_2 f(A_s)[C_2H_2] \tag{9}$$

The function $f(A_s)$ incorporates the dependence of soot surface growth on the soot surface area per unit volume, A_s. Proposed forms of $f(A_s)$ include: $f(A_s) = A_s^{0.5}$ [54] and $f(A_s) = A_s$ [55]. Here we have used the first relationship to account for particle aging and surface site deactivation [21,74,75]. The corresponding rate constants, k_1 and k_2, are given by [73]

$$k_1 = 1000\exp(-16103/T) \tag{10}$$

$$k_2 = 1750\exp(-10064/T) \tag{11}$$

Surface area is related to the soot mass and number density by

$$A_s = \pi\left(\frac{6}{\pi}\frac{1}{\rho_s}\frac{Y_s}{N_s}\right)^{2/3}(\rho N_s) \tag{12}$$

where ρ_s is the density of soot, taken to be 1900 kg/m^3. The oxidation reaction rates per unit surface area are modeled by [21]

$$R_3 = 120\left\{\frac{k_a p_{O_2}\chi}{1+k_z p_{O_2}} + k_b p_{O_2}(1-\chi)\right\} \tag{13}$$

$$R_4 = \varphi_{OH} k_4 T^{-1/2} p_{OH} \tag{14}$$

$$R_5 = \varphi_O k_5 T^{-1/2} p_O \tag{15}$$

where

$$\chi = \left\{1 + \frac{k_T}{k_b p_{O_2}}\right\}^{-1} \tag{16}$$

The symbols p_{O_2}, p_{OH} and p_O denote the partial pressures of O_2, OH and O in atm , respectively. The collision efficiencies for OH, φ_{OH}, and O, φ_O, were both assumed equal to 0.2. The rate of soot oxidation by O_2 was based on the Nagle–Strickland–Constable model [76] with the rate constants k_a, k_b, k_z, k_T, and k_4 taken from Moss et al. [77]. The rate constant k_5 was equal to the value used by Bradley et al. [78].

The source term in (2) represents the production and destruction of the soot particle number density with nucleation and agglomeration. It is modeled herein as follows:

$$S_N = \frac{2}{C_{min}} N_a R_1 - 2C_a\left(\frac{6M_s}{\pi\rho_s}\right)^{1/6}\left(\frac{6k_B T}{\rho_s}\right)[C(s)]^{1/6}(\rho N_s)^{11/6} \tag{17}$$

where N_a is Avogadro's number 6.022×10^{26} kmol^{-1}, k_B is the Boltzmann constant 1.38×10^{-23} m^2 kg s^{-2} K^{-1}, $C_{min} = 700$ is the number of carbon atoms in the incipient carbon particle, C_a is the agglomeration rate constant, and $[C(s)] = \rho Y_s/M_s$ is the molar concentration of soot. Based on the recommendations of Liu et al. [21] and Ezekoye and Zhang [48], coalescence was neglected by setting C_a to zero. This means that particles stick together when they collide and that the total particle surface area is not changed by the collision.

Several issues related to numerical stability and convergence were encountered using the previously described soot model. First, both S_Y and S_N are functions of Y_s and N_s raised to sub-unity powers. For example,

$$S_Y \propto Y_s^{1/3} N_s^{1/6} \quad \text{and} \quad S_N \propto Y_s^{1/6} \tag{18}$$

As a result, derivatives of S_Y and S_N with respect to Y_s or N_s become infinite as $Y_s \to 0$ or $N_s \to 0$. Additionally, oscillations in Y_s or N_s caused by round-off and numerical diffusion errors can produce large fluctuations in the source terms when Y_s and N_s are small. Both of these issues caused the Newton–Krylov time-marching algorithm applied herein to stall. To overcome this stall, A_s was modified by applying a blending function to eliminate any on/off switching experienced by S_Y and smooth its derivative with respect to Y_s and N_s. The modified surface area is given by

$$A_s^* = \beta(Y_s)\beta(N_s)A_s \tag{19}$$

where the blending function, $\beta(x)$, is defined as

$$\beta(x) = 1.0 - \exp\left[-5\left(\frac{x}{10^{-6}}\right)^2\right] \tag{20}$$

The modification was applied by replacing A_s with A_s^* in (7) and (9).

2.2. Radiation model

Radiation emitted and absorbed by both the gas and soot is modeled using the discrete ordinates method (DOM) coupled with the point-implicit finite volume approach of Carlson and Lathrop [79]. Spatial derivatives are evaluated using centered differences while ordinate directions and weights were selected based on the T_3 quadrature set [80]. Spectral absorption coefficients are approximated using a wide-band model which is based on the statistical narrow-band correlated-k (SNBCK) model [81]. Four Gauss quadrature points were found to provide a reasonable balance between accuracy and computational expense when integrating the DOM equations over each band [82,83]. In this work, the narrow-band data of Soufiani and Taine [84] for H_2O, CO_2 and CO are used to construct the cumulative distribution function. To reduce the number of unknowns required for non-gray radiation in mixtures, the three radiating gases are approximated by a single gas with effective narrow-band parameters based on the optically thin limit [85]. Additional computational savings are achieved by combining bands to form several wide bands using the lumping procedure described by Liu et al. [81]. Based on the recommendations of Goutiere et al. [86], a total of nine non-uniformly spaced wide bands are employed. The spectral absorption coefficient for soot is determined based on the Rayleigh limit for small spherical particles [73].

2.3. Solution procedure

The equations governing the gas-particle mixture described previously are solved numerically using a finite-volume scheme previously developed by Groth and co-workers [67,87,88]. The scheme makes use of piecewise limited linear reconstruction and an approximate Riemann solver to determine the inviscid fluxes [89]. The second-order diamond-path method developed by Coirier and Powell [90] was used to compute the viscous fluxes. Both the inviscid flux and the temporal derivative are preconditioned using the proposed matrix of Weiss and Smith [91]. This preconditioning helps reduce excessive dissipation and numerical stiffness commonly encountered when applying the compressible gas equations to low-Mach-number flows. The solution of the fully-coupled nonlinear ODEs are relaxed to a steady-state using the block-based parallel implicit algorithm developed by Northrup and Groth [87] which makes use of a matrix-free inexact Newton–Krylov method. Solution of the DOM equations is decoupled from the gas-particle flow equations and solved sequentially at each time step.

Thermodynamic and transport properties along with gas-phase kinetic rates are evaluated using CANTERA [92], an open-source software package for chemically-reacting flows. The simulations were performed using a modified version of the Gri-Mech 3.0 mechanism for CH_4 combustion [93]. Nitrogen was assumed to be inert and all reactions and species related to NO_x formation were removed from the mechanism, giving a final reduced mechanism with 36 species and 219 reactions.

3. Coflow burner configuration and problem formulation

The burner configuration and operating conditions are described in detail by Thomson et al. [18] and Joo and Gülder [20]. The burner consists of a central fuel tube with a 3 mm exit diameter and a concentric coflow-air tube with a 25.4 mm inner diameter. It was installed inside a pressure vessel which allowed the flame operating pressure to be varied as desired. Both the inner and outer surfaces of the fuel tube are chamfered with a round edge at the nozzle exit plane. A chimney with an inner diameter of 25.4 mm was used to improve flame stability by

shielding the core flow from disturbances created inside the chamber. For all the flames, constant mass flow rates for methane and air of 0.55 mg/s and 0.4 g/s were maintained, respectively, which corresponds to an equivalent carbon flow rate of 0.412 mg/s. Exactly the same burner and flow rates were used in the numerical study of Liu et al. [21]. Joo and Gülder obtained measurements for temperature and soot volume fraction in flames at pressures between 10 and 60 atm under normal-gravity conditions. In the present study, calculations were performed at pressures ranging from 1 to 60 atm both with and without gravity. The temperature of the fuel and air supplied to the burner was assumed to be equal to 300 K for all cases.

3.1. Computational domain and mesh

The two-dimensional computational domain used herein for the coflow burner is shown schematically in Fig. 1 along with the applied boundary conditions. The domain extends radially-outwards 20 mm and 25 mm downstream. The modeled domain is also extended 9 mm upstream into the fuel and air tubes to account for the effects of fuel preheating [94] and better represent the inflow velocity distribution. Increasing the size of the domain further had no effect on the solution. Note that the domain was extended radially beyond the chimney walls to improve numerical convergence. This alteration had no affect on the predicted flowfield surrounding the flame since the chimney walls are far away from the flame. A simplified representation of the fuel tube geometry was employed to reduce the numerical complexity of this particular problem. As shown in Fig. 1, the chamfered edge of the fuel tube was approximated by a tube with 0.4 mm uniformly-thick walls.

The computational domain illustrated in Fig. 1 was subdivided into 192 cells in the radial- and 320 in the axial-direction to form a structured, non-uniformly-spaced mesh with 60,000 cells. These cells were clustered towards the burner exit plane to capture interactions near the fuel tube walls and towards the centerline to capture the core flow of the flame. A fixed mesh spacing of approximately 35 μm was specified in the radial-direction between $r = 0$ and $r = 4.8$ mm. The vertical spacing approaches 5.6 μm near the fuel tube exit plane. The same mesh was employed for all calculations, zero- and normal-gravity, to facilitate the comparison. Increasing the mesh resolution did not significantly improve the numerical solution.

All computations were performed on a high performance parallel cluster consisting of 104 IBM P6-575 nodes with 128 GB RAM per node and a high-speed interconnect. The nodes each have 32 IBM POWER6 cores (4.7 GHz) and are connected to a non-blocking switch with four 4×-DDR InfiniBand links.

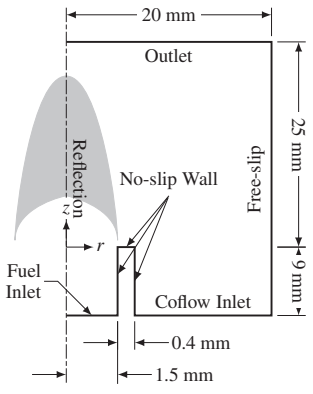

Fig. 1. Computational domain and boundary conditions.

3.2. Boundary conditions

The far-field boundary was treated using a free-slip condition. At the outlet, temperature, velocity, species mass fractions and soot number density are extrapolated while pressure is held fixed. The gas/soot mixture composition, velocity, and temperature are prescribed at the inlet while the inlet pressure is extrapolated from inside the domain. Uniform velocity and temperature profiles were applied for both the fuel and air inlet boundaries. The three surfaces that lie along the tube wall were modeled as adiabatic walls with zero-slip conditions. For the radiation solver, all boundaries except for the axis of symmetry are assumed to be cold and black.

All of the flames considered in this study are stabilized by the burner tube rim. As a result, significant heat transfer occurs between the flame and tube that causes the temperature of the tube surface to increase. This heat transfer intensifies with increasing pressure as the flame base moves towards the burner rim and temperature gradients near the burner steepen [18]. Gülder et al. [95] measured tube surface temperatures as much as 100 K higher than ambient conditions for similar laminar coflow diffusion flames at atmospheric pressure. They concluded that the heat transfer between the fuel tube and hot gases significantly affects local gas temperatures and soot volume fractions.

Most numerical studies involving burner-stabilized laminar coflow diffusion flames employ fixed-temperature boundary conditions and assume that the tube temperature is equal to that of the cold reactants [21,63,75]. These studies also neglect any increase in fuel or oxidizer temperature upstream of the burner exit plane. One exception is the study by Guo et al. [94] which captured the preheating effect by including the upstream portion of the burner and prescribing a temperature distribution along the burner walls. Specifying cold walls represents the limit in which absolutely no heating of the tube occurs whereas the adiabatic conditions used here represent the opposite limit for the effect of gas-tube heat transfer—that is, the tube is allowed to heat up to the maximum possible temperature. Based on prior experimental [95,96] and numerical [94] findings, it is clear that accurate representation of laminar diffusion flames requires incorporating conjugate heat transfer between the gas and tube wall. However, such an analysis can be computationally demanding and is beyond the scope of this study.

Several investigators artificially increased the prescribed temperatures at the inlet (fuel, air, and tube surface) to improve the agreement between predictions and experimental measurements [62,83]. However, this type of trial-and-error analysis is not ideal for large systematic studies with varying operating conditions. Guo et al. [94] found that predictions for temperature and soot volume fraction improved when the upstream portion of the tube was modeled with an experimentally-measured temperature distribution prescribed along the tube walls. However, experimental data for the tube temperature is not available for the flames studied here and the measurements obtained by Gülder et al. [95] are not applicable. Temperature increases in the tube wall are expected to be much larger in the present study, especially at higher pressures where the flame almost touches the burner rim [18,20].

Preliminary calculations for the normal-gravity flames were first attempted using prescribed cold-wall boundary conditions. However, the predictions did not accurately represent the experimental results above 20 atm. For these cases at pressures above 20 atm, converged steady-state solutions could not be obtained and, in some cases, the flames descended into the fuel tube. Nor could a suitable temperature distribution along the tube wall be prescribed that mimicked the experimental results. As such, adiabatic wall conditions were chosen for the entire study as they provided the best agreement between numerical predictions and

experimental measurements. The same adiabatic boundary conditions were prescribed for the zero-gravity flames.

4. Verification with measurements

4.1. Numerical convergence for high-pressure flames

In general, the Newton–Krylov algorithm converged well and relatively quickly for all cases at low pressures, but unfortunately stalled at pressures of 30 atm and above when gravity was present. This convergence stall was attributed to the decreasing flow speeds and increasing ODE stiffness which occurred as pressure increased. The stiffness of the governing ODEs increased significantly with pressure as gas-phase and soot-related reaction rates intensified. Several solutions were employed to avoid convergence stall. First, a relaxation factor of 0.1 was applied to the non-linear Newton update computed at each outer iteration. Second, the soot number density was taken to be constant and the corresponding transport Eq. (2) was not solved, further alleviating numerical stiffness. A similar approach was applied by Kennedy et al. [71] for the numerical prediction of soot in ethylene laminar diffusion flames. They found that the predicted soot volume fractions were relatively insensitive to the assumed number density provided that the production of soot mass was dominated by surface growth mechanisms. Based on their work, a constant number density of 10^{18} kg^{-1} was assumed for the 30, 40, 50 and 60 atm flames at normal-gravity. The maximum predicted values for the soot number density in the 1, 10 and 20 atm normal-gravity flames are $0{:}46 \times 10^{18}$, $1{:}33 \times 10^{18}$ and $1{:}47 \times 10^{18}$ kg^{-1}, respectively. With these modifications, converged steady-state solutions were obtained in all cases. These modifications were not required for the zero-gravity flame calculations as no numerical difficulties were encountered. They were only employed for calculations of the normal-gravity flames between 30 and 60 atm.

4.2. The implications of assuming a constant number density

Two separate tests were conducted to assess the implications of assuming a constant number density as described previously on soot volume fraction predictions. First, calculations for the normal-gravity flames were performed at 1, 10 and 20 atm assuming a constant number density of 10^{18} kg^{-1} and the results were compared to those obtained by solving (2). Comparing the two sets of predictions, Fig. 2a, the constant number density assumption has negligible effect on the predicted soot volume fraction. The largest differences between solutions occur at 1 atm where soot volume fractions are low. Based on these results, assuming a constant N_s is not expected to significantly affect the predictive accuracy of the soot model above 1 atm.

The second test consisted of comparing the results obtained for the 20 atm normal-gravity flame assuming different values for N_s. As illustrated in Fig. 2b, which compares the predicted contours for soot volume fraction obtained using three different values of N_s, the solution is only sensitive to the assumed value of N_s when N_s is small. For example, increasing N_s by a factor of 100 from 10^{18} to 10^{20}kg^{-1} produced a 5% increase in the peak soot volume fraction. However, a 33% decrease results from a 100-fold decrease in N_s from 10^{18} to 10^{16} kg^{-1}. These results indicate that the soot model is fairly insensitive to N_s as long as a reasonable estimate for N_s is provided.

For the remainder of this study, calculations for all flames except the normal-gravity flames between 30 and 60 atm included the solution of (2). The modifications discussed in Section 4.1, which include the assumption of a constant number density for soot, were only applied to the 30–60 atm normal-gravity flames.

4.3. Radial profiles

The predicted radial profiles of soot volume fraction at various heights above the burner are compared with the measurements of Joo and Gülder [20] in Fig. 3. Only the numerical results obtained for the normal-gravity flames are presented in the figure. The model predicts many of the experimentally observed trends but tends to over-predict the soot volume fraction throughout the flames. In both the experiments and calculations, soot is formed in an annulus downstream of the fuel tube rim and the soot volume fractions initially increase with height. The locations of the peaks within this annulus converge towards the centerline as the inner accelerating core flow entrains the soot particles inwards. Oxidative processes begin to convert soot to gaseous species such as CO higher up in the flame, causing soot levels to drop. As pressure is increased, the peaks in the radial profiles for soot volume fraction become more pronounced and their locations contract radially-inwards. Soot production also increases with pressure since the higher pressures and contracting flame result in higher gaseous species concentrations, larger mixture densities and faster reaction rates. While these features are observed in the numerical results, the magnitude of the predicted soot volume fraction is greatly over-predicted in most cases, especially in the annular region with high soot levels. For example, the peak soot concentrations for the 10 atm flame are over-predicted by factors of 2.2, 1.7 and 2.5 at axial heights of 3, 5 and 7 mm, respectively. This agreement does not improve much as pressure is increased to 60 atm where the peaks are over-predicted by factors of 1.6, 1.4 and 2.8 at the 2, 5 and 8 mm heights, respectively. Along the centerline, the concentration of soot is under-predicted for the 10 and 20 atm flames and is consistently over-predicted for the other flames.

The predicted annular regions of high soot concentration in Fig. 3 are much thicker than the measured values and the locations of the predicted peaks are shifted radially-inward. One possible cause of the thicker predicted annular soot-containing region is errors introduced by the simplified representation of the PSD, but

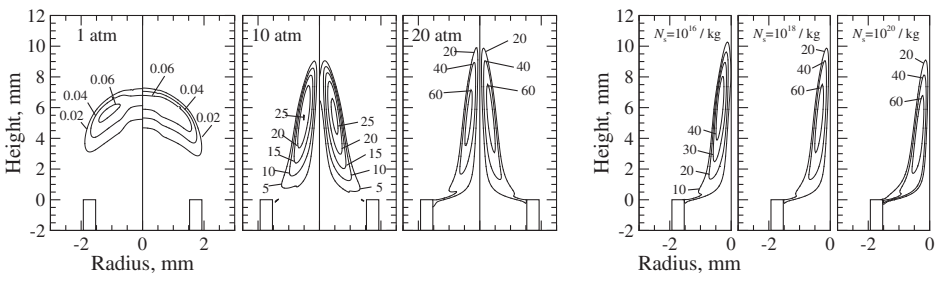

(a) Left: solving Eq. (2); Right: assuming N_s = 10^{18} kg^{-1}. (b) Effect of constant number density.

Fig. 2. Effect of number density on predicted contours for soot volume fraction in the normal-gravity flames. Units in ppm.

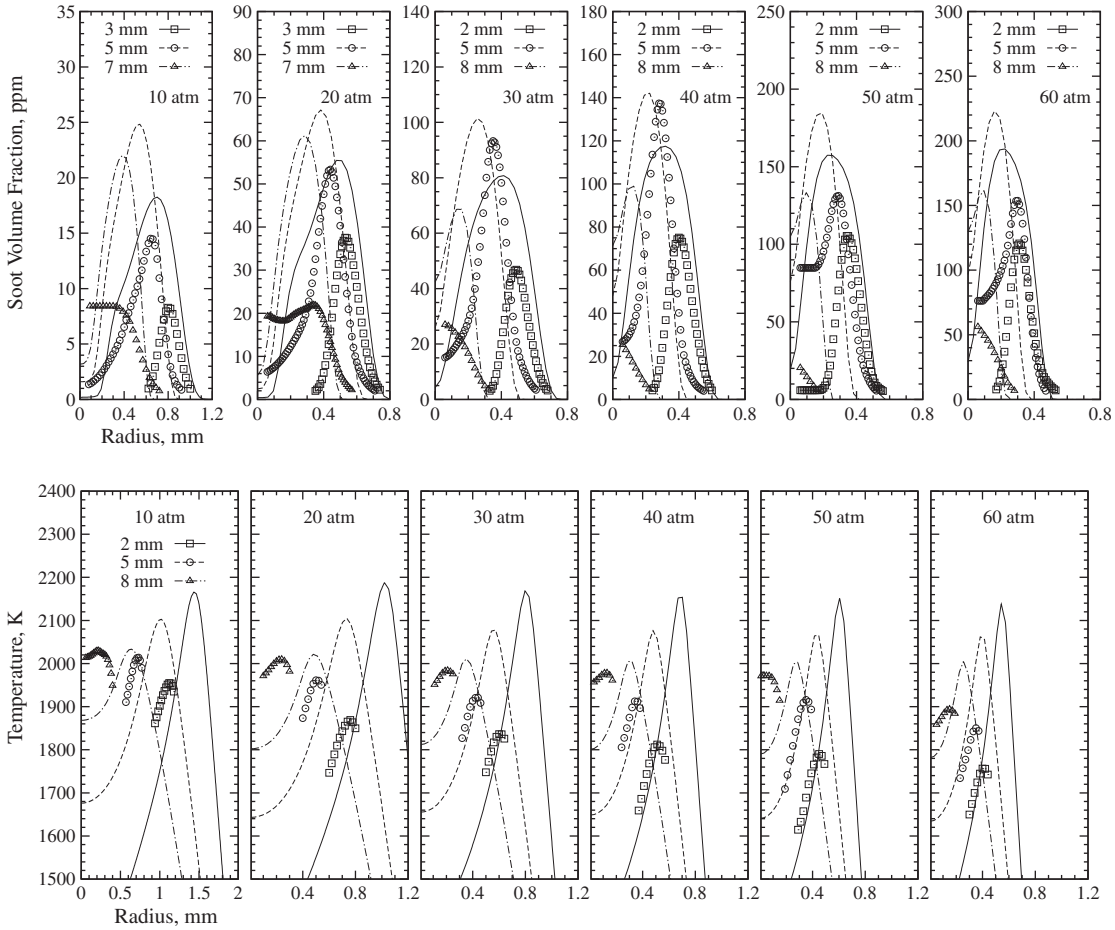

Fig. 3. Measured (symbols) and predicted (lines) radial profiles for soot volume fraction and temperature. Measurements taken from Joo and Gülder [20].

these discrepancies could also be caused by errors in the soot chemistry sub-model. The shifted locations of the predicted peaks are attributed to the simplified geometrical representation of the burner rim.

While many of the trends with pressure and flame height can be observed in both the numerical and experimental results depicted in Fig. 3, some trends are incorrectly predicted. Temperature has an annular structure similar to the radial profiles for soot volume fraction except that the radial location where temperature peaks occurs at a slightly larger radius. With increasing height in the flames, the experimental results show an increase in the peak temperature which gradually shifts in position towards the centerline. This radially-inward shift of the peaks is correctly predicted, although the calculated peak temperatures decrease with downstream distance. This indicates that the predicted peak temperature occurs much lower in the flames than in the experiments. Higher temperatures low in flame where there is an abundance of fresh fuel would result in larger soot formation rates and cause the over-predicted soot volume fractions previously discussed.

As pressure is increased, the measured temperature profiles contract inwards and the peaks become more pronounced. Increasing pressure is also observed to result in a slight decrease in the peak temperatures at each height as more soot is produced and radiative heat losses to the surroundings intensify. While the predictions show these same trends with pressure, the decrease in peak temperature with increasing pressure is not as severe. This suggests that the relationship between soot yield and pressure is incorrect because soot volume fraction and temperature are tightly coupled through radiation. Since radiation from soot can have a strong effect on flame temperature [73,97,98], the disagreement in the relationship between the peak flame temperatures and pressure may be caused by errors introduced by the soot model.

Temperature predictions in the lower portion of the flame at 2 and 5 mm agree reasonably well with the measurements, except that the peaks are over-predicted. Higher in the flame at 8 mm, the peak values are in better agreement with the experimental data except shifted radially-outward, especially for pressures between 10 and 40 atm. There is also a significant under-prediction of temperature along the centerline closer to the tip of the flame. Peak temperatures at the lowest axial height, where their agreement is poorest, are greatly over-estimated by 210 K at 10 atm, 310 K at 20 atm, 325 K at 30 atm, 340 K at 40 atm, 387 K at 50 atm and 370 K at 60 atm. The high temperatures near the burner are a result of the adiabatic boundary condition over-predicting wall temperatures. The under-predicted temperatures along the centerline at the higher heights are a result of the thicker soot regions and larger soot yield that were predicted, observed in Fig. 3, which increase radiative heat losses from the core of the flame. The shifted temperature profiles are most likely caused by the simplified geometry.

4.4. Soot volume fraction contours

Predicted contours of soot volume fraction are presented alongside those constructed from the measurements of Joo and Gülder [20] in Fig. 4. Qualitatively, the predicted and measured flame geometries are similar and the narrowing of the flame with increasing pressure is clearly observed in both sets of results. The

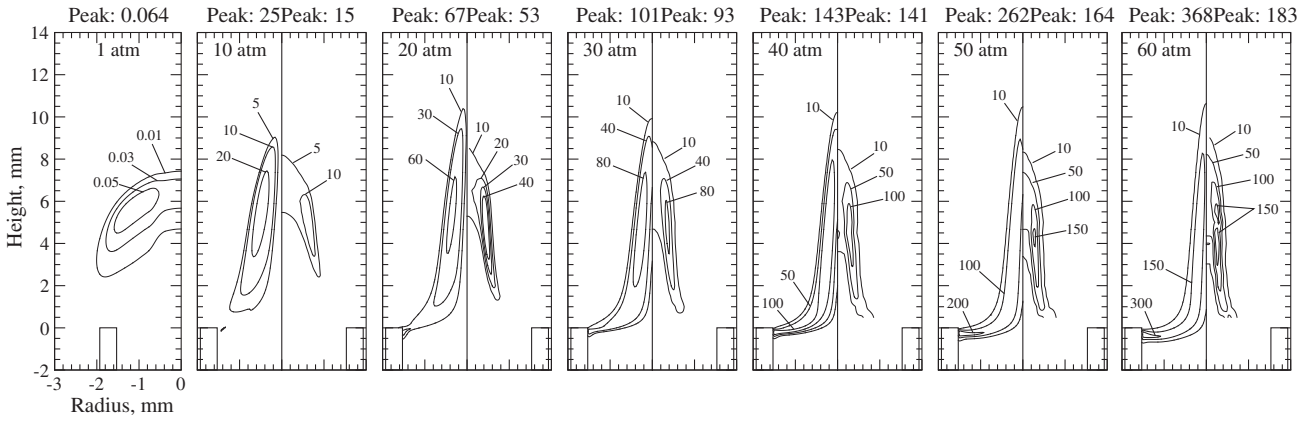

Fig. 4. Predicted (left) and measured (right) contours for soot volume fraction in ppm. Measurements taken from Joo and Gülder [20].

flame height based on soot volume fraction is over-predicted for each pressure, but remains constant at approximately 11 mm between 20 and 60 atm. Decreasing pressure below 20 atm caused the predicted flame height to decrease to 10 mm at 10 atm and 7.5 mm at 1 atm. These numerical predictions for flame height are based on the location where the soot volume fraction is equal to 0.01 ppm. In contrast, a constant visible flame height of 9 mm was observed in the experimental results. Similar numerical results for flame height were obtained by Liu et al. [21] for the same flames, although they predicted a more agreeable constant flame height of 9.5 mm.

The model correctly predicts the general vicinity of the peak soot volume fraction, however, some significant differences between predicted and measured soot concentrations are observed in Fig. 4 at lower flame heights. For instance, the model always predicts that soot production begins further upstream than in the experiments. With increasing pressure, both experiments and predictions show that the initial onset of soot formation begins earlier and that the annular structure becomes thinner and more pronounced. Beginning at 10 atm, the model predicts a small amount of soot inside the fuel tube near the wall that intensifies as pressure is increased further to 60 atm. Soot concentrations inside the tube begin to approach the maximum levels for the whole flame around 30 atm and exceed the values which occur higher up in the 50 and 60 atm flames. These results for the predicted soot volume fraction are different from those presented by Liu et al. [21], who predicted much lower soot concentrations in better agreement with the experimental results for the same flames between 10 and 40 atm. They did not predict such high soot concentrations near the burner rim.

The differences between the numerical results obtained in this study and those presented by Liu et al. [21] are mainly attributed to the different wall boundary conditions employed: fixed-temperature versus adiabatic. Both studies used a similar numerical model with only a few differences: (1) Liu et al. did not model upstream of the burner exit; and (2) in this study, the unmodified equations governing compressible gas mixtures were solved instead of the low-Mach-number equations. As a result, Liu et al. were able to obtain realistic steady-state solutions for the normal-gravity flames between 5 and 40 atm with cold-wall boundary conditions and without requiring the constant number density approximation. Based on the results discussed in Section 4.2, the constant number density approximation is not expected to significantly affect the predictions. Rather, the adiabatic boundary conditions are assumed responsible for high predicted temperatures near the burner which causes soot formation to occur lower in the flame. Higher overall soot concentrations and longer flame heights occur as a result. While the adiabatic wall boundary condition may be somewhat inaccurate, the resulting solutions better represent the physical behavior of the flames when compared to solutions obtained assuming a fixed, low-temperature wall. As discussed in Section 3.2, physically realistic solutions could not be obtained above 20 atm with cold-wall boundary conditions. There is some experimental support for high soot concentrations predicted within the fuel tube near the exit [99,100]. Using the same set-up, Mandatori and Gülder [99] observed the complete blockage of the fuel tube by soot at about 35 atm with an ethane diffusion flame. Similarly, Joo and Gülder [100] observed the discharge of carbon particulates along with a liquid phase from the fuel nozzle of high-pressure methane–air coflow diffusion flames.

4.5. Soot yield

To assess the fuel's propensity to soot and its sensitivity to pressure, the variation in the carbon conversion factor with pressure was studied. This factor is defined as $\eta_s = \dot{m}_s/\dot{m}_c$, where $\dot{m}_c$ is the carbon mass flow rate at the nozzle exit [16]. The mass flux of soot through a horizontal cross-section is

$$\dot{m}_s = 2\pi\rho_s \int f_v v r \, dr \tag{21}$$

where ρ_s = 1.9 g cm^3 is the density of soot [73], f_v is the soot volume fraction and v is the axial velocity. Since the velocity is not known in the experiments, it is estimated by $v = \sqrt{2az}$, where z is the height above the burner and a is an acceleration constant commonly assumed equal to 25 m/s^2 [23]. The computed velocity was also used as an alternative to estimate $\dot{m}_s$ in (21) using the experimentally-measured soot volume fractions.

The results for the maximum carbon conversion factor based on the experimental measurements are compared with the numerical predictions in Fig. 5. The numerical results obtained for the

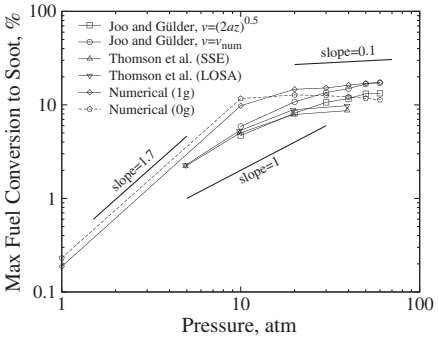

Fig. 5. Maximum fuel carbon converted to soot as a function of pressure.

zero-gravity flames are discussed in detail in the following section. Experimental results based on measurements obtained by Thomson et al. [18] using both line-of-sight attenuation (LOSA) and spectral soot emission (SSE) are also displayed in the figure. Note that the results reported by Thomson et al. were derived using the $v = \sqrt{2az}$ approximation. Differences between the measurements reported by Thomson et al. and Joo and Gülder above 20 atm were attributed to systematic calibration errors in the fuel flow rate introduced by Thomson et al. at high pressures [20].

As observed in Fig. 5, there is a significant difference between the two lines corresponding to the experimental results of Joo and Gülder based on the different velocity approximations. The values computed using the predicted velocity field are assumed to be more accurate.

The predictions for the normal-gravity flames mimic the experimentally observed trends reasonably well, but the maximum η_s in each flame is consistently over-predicted. The degree of this over-prediction diminishes as pressure is increased to 60 atm. For example, the peak carbon conversion is over-predicted by a factor of 1.7 at 10 atm, a factor of 1.1 at 40 atm, and correctly predicted at 50 and 60 atm. Both the experimentally-based and predicted maximum values for η_s display a dependence on pressure that weakens as pressure is increased from 10 to 60 atm. However, the numerical predictions over-predict the slope at pressures below 10 atm and under-predict the slope above 10 atm. A slight discontinuity occurs in the predicted relationship between η_s and pressure at 30 atm where the soot model modifications for improved convergence were applied. Despite the modeling changes, the numerical results still predict the correct trends. This would suggest that the majority of the total soot mass is produced through surface reactions.

5. Effects of gravity and pressure

5.1. Soot yield

Eliminating gravity has a large effect on the predicted maximum η_s, Fig. 5. In the low-pressure flames at 1 and 10 atm, removing gravity enhances the maximum η_s by about a factor of 1.2 but does not alter the relationship between η_s and pressure within this range. However, the predictions for the two gravity levels begin to deviate significantly above 10 atm since increasing pressure further causes η_s to decrease for zero-gravity and increase for normal-gravity. As a result, η_s is lower in the zero-gravity flames for high pressures.

The differences observed between the η_s-pressure relationships at the two levels of gravity are partially explained by comparing the local variation of the soot mass fraction along a soot particle's path, shown in Fig. 6 for each flame. In the figure, the trajectory of the soot particle originates at the reaction zone and passes through the region of maximum soot volume fraction. The reaction zone was designated by the location where the mixture fraction is stoichiometric. A similar procedure was performed by Honnery and Kent [101,102] to analyze experimental measurements in laminar diffusion flames of ethylene and ethane.

For this numerical study, the mixture fraction was computed using the following relation proposed by Bilger [103] for methane–air flames:

$$Z = \frac{2Y_C/M_C + \frac{1}{2}Y_H/M_H + (Y_{O,2} - Y_O)/M_O}{2Y_{C,1}/M_C + \frac{1}{2}Y_{H,1}/M_H + Y_{O,2}/M_O} \tag{22}$$

From (22), the stoichiometric value of Z is equal to

$$Z_{st} = \frac{Y_{O,2}/M_O}{2Y_{C,1}/M_C + \frac{1}{2}Y_{H,1}/M_H + Y_{O,2}/M_O} \tag{23}$$

where Y_j and M_j are the mass fractions and atomic masses for the elements carbon, hydrogen and oxygen. Subscripts 1 and 2 refer to values in the fuel and air streams, respectively.

The local variation of Y_s along a soot particle's path for each flame is shown in Fig. 6. The normal-gravity flames at 50 and 60 atm could not be analyzed in this manner due to difficulties defining a particle trajectory. Difficulties arose because the maximum soot volume fractions for these two flames occurred inside the tube instead of further downstream above the burner rim. The most noticeable difference between the results for the two gravity levels is that particle residence time in the normal-gravity methane flames initially increases with pressure from 1 to 10 atm, but then remains approximately fixed for further increases in pressure beyond 10 atm. This means that the flames above 10 atm are fully developed and that the residence times for these flames are independent of pressure, which corresponds with the theory described in Section 1. The pressure beyond which residence times stop increasing, 10 atm, corresponds with the drastic change in the pressure-η_s relationship observed in Fig. 5 for the normal-gravity flames. Similar behavior is observed at zero gravity, except that the peak soot mass fractions begin to decrease above 20 atm even though particle residence times continue to increase.

As can be seen in Fig. 7, pressure has differing effects on the predicted contours of soot mass fraction at the two levels of gravity. At 1 atm, the structure of the predicted contours for both levels of gravity are similar because the effects of buoyancy in the normal-gravity flame are relatively small. Soot concentrations are

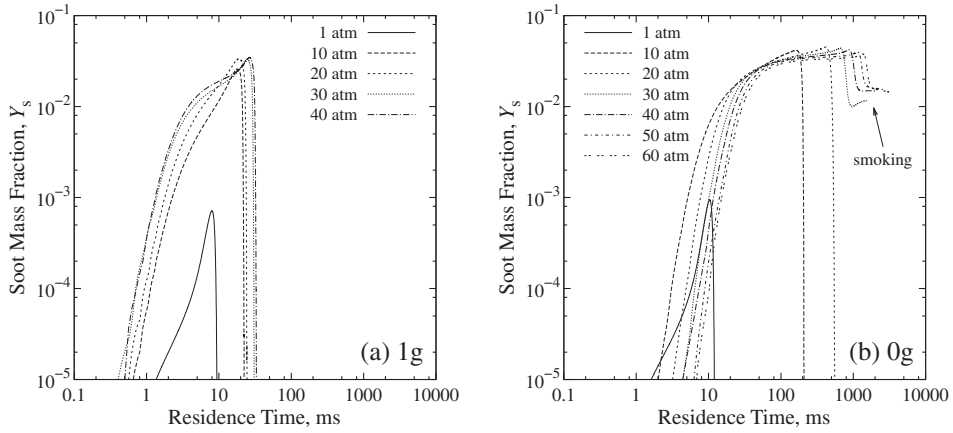

Fig. 6. Soot mass fraction along a particle streamline originating from the reaction zone and passing through the maximum soot volume fraction for (a) normal- and (b) zero-gravity flames.

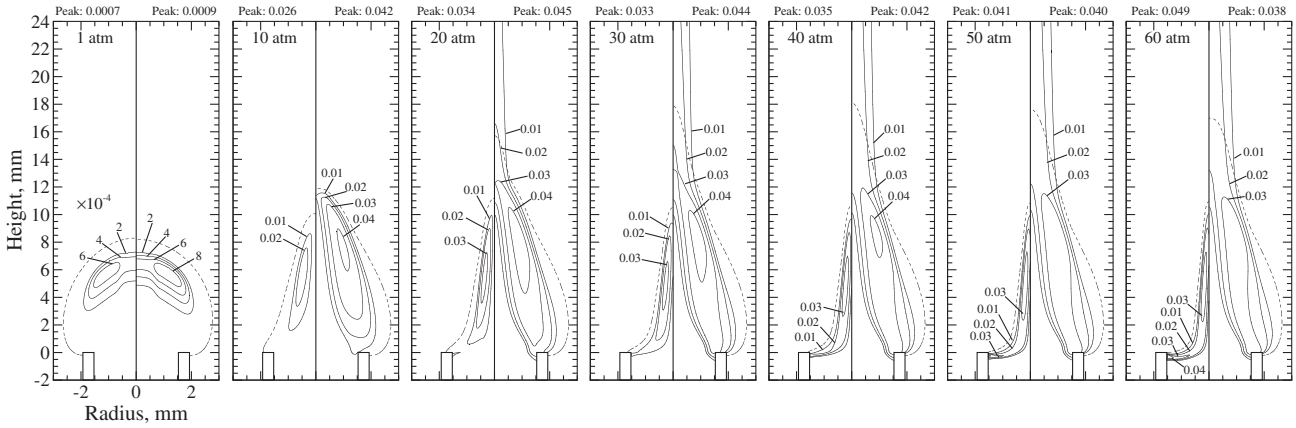

Fig. 7. Predicted contours for soot mass fraction in the normal-gravity (left) and zero-gravity (right) flames. Dashed black lines denote the location where the mixture fraction is equal to the stoichiometric value.

higher and the onset of soot occurs lower in the zero-gravity flame since residence times are longer. As pressure is increased, buoyant forces distort the flow, pulling streamlines towards the centerline and causing the normal-gravity flames to narrow. This narrowing increases temperatures along the centerline and enhances the production of soot. Since both radial velocities and reaction rates increase as pressure is increased in the presence of gravity, the reaction zone narrows and the annular soot zone becomes thinner in the normal-gravity flames.

When gravity is neglected, velocities decrease linearly with pressure while the streamlines remain unaffected. Therefore, soot production increases with pressure in the zero-gravity cases primarily because the residence times are longer and the entrainment of fresh oxidizer into the flame is slower. However, longer residence times and higher soot concentrations promote radiation losses and, as a result, temperatures in the zero-gravity flames decrease with pressure, Fig. 9a. In addition to this, the amount of available acetylene for further soot production declines as pressure is increased and more soot is produced, Fig. 12a. Declining acetylene concentrations are also observed when soot and radiation are neglected in the calculations, Fig. 12b, but at a much slower rate. This indicates that changes in chemistry at high pressure results in less acetylene available to produce soot under zero-gravity conditions. At some critical pressure, around 30 atm in this study, the combined effects of low temperatures and reduced acetylene concentrations in the zero-gravity flames begin to negatively affect soot formation rates. This results in the declining soot mass fractions observed in Figs. 6 and 7 for the zero-gravity flames as pressure is increased above 30 atm.

Once pressure is increased to 20 atm, the zero-gravity flames begin smoking. Soot concentrations increase significantly with pressure between 1 and 20 atm regardless of gravity level, but the convective transport of oxygen to the flame is much lower in zero-gravity. In addition, temperatures in the zero-gravity flames are drastically lowered by radiation at high pressures. Both contribute to slow oxidation rates in zero-gravity.

There is a noticeable difference in the effect of pressure on flame structure at the two gravity levels. Under normal-gravity, the annular soot-containing region becomes thinner and more pronounced as pressure is increased to 60 atm. However, thermophoretic forces become important in zero-gravity, especially at high pressures where flow velocities are low, driving particles off flow streamlines and thickening the annular soot-containing region. The increased effects of molecular diffusion, which also become relatively more important as pressures are increased in the absence of gravity, contribute to the thickening of the soot-containing region by widening the reaction zone.

5.2. Residence time and velocity

The axial velocity along centerline, illustrated in Fig. 8a for all flames, steadily decreases with increasing pressure under zero-gravity conditions. While there is a small decrease in axial velocity between the 1 and 10 atm normal-gravity flames, there is almost no change above 10 atm. This pressure corresponds to the pressure above which the particle residence time stops increasing.

The mass flow rate through the stoichiometric flame envelope is shown in Fig. 8b for all flames. For this study, the flame envelope is defined by the isocontour where the mixture fraction is stoichiometric. The mass flow decreases beyond about 3 mm since the flame begins to close. The mass flow rate through the normal-gravity flames first increases from 1 to 10 atm, but then remains roughly constant for all pressures above this. This means that the amount of air entrained into the flame does not increase above 10 atm. However, the rate of entrainment does appear to increase with pressure at normal gravity since the initial slopes of the lines in Fig. 8b become steeper. The mass flow through the zero-gravity flames is much lower, except at 1 atm, and does not change much as pressure is increased. This is one of the causes for the higher smoking propensity observed in zero-gravity as there is less oxygen entrained into the flame even though soot production is enhanced.

5.3. Temperature and radiation heat transfer

While there is almost no difference between the predicted temperature contours of the zero- and normal-gravity flames at 1 atm, Fig. 9a, the significant changes that occur as pressure is increased cause large deviations at high pressure. In zero-gravity, enhanced radiation losses resulting from the long residence times and high soot volume fractions reduce local gas temperatures steadily as pressure is increased. This observed decrease in temperature is especially pronounced along the centerline, causing a shift in the location of the peak temperature from the tip of the flame to the base. This shift does not occur in the normal-gravity flames and, in general, different behavior is observed when gravity is turned on. Instead, buoyant forces contract the flame while enhanced convective transport and high pressures promote fast reaction rates and thin reaction zones.

A considerable degree of preheating is observed along the centerline at high pressures and normal-gravity levels while fuel preheating is negligible in zero-gravity. Instead, the air stream is preheated near the tube wall in the zero-gravity flames. Both of these observed preheating effects are assumed to be somewhat artificially enhanced by the adiabatic wall conditions.

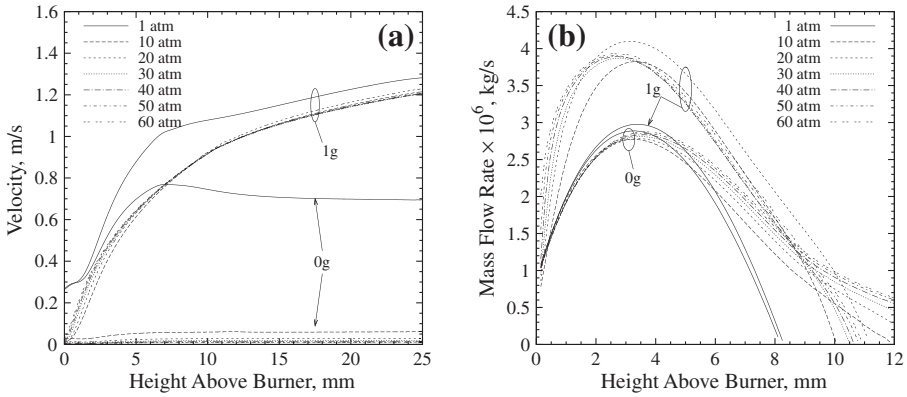

Fig. 8. Distributions of the predicted axial velocity along the flame centerline and the mass flow rate through the stoichiometric flame envelope.

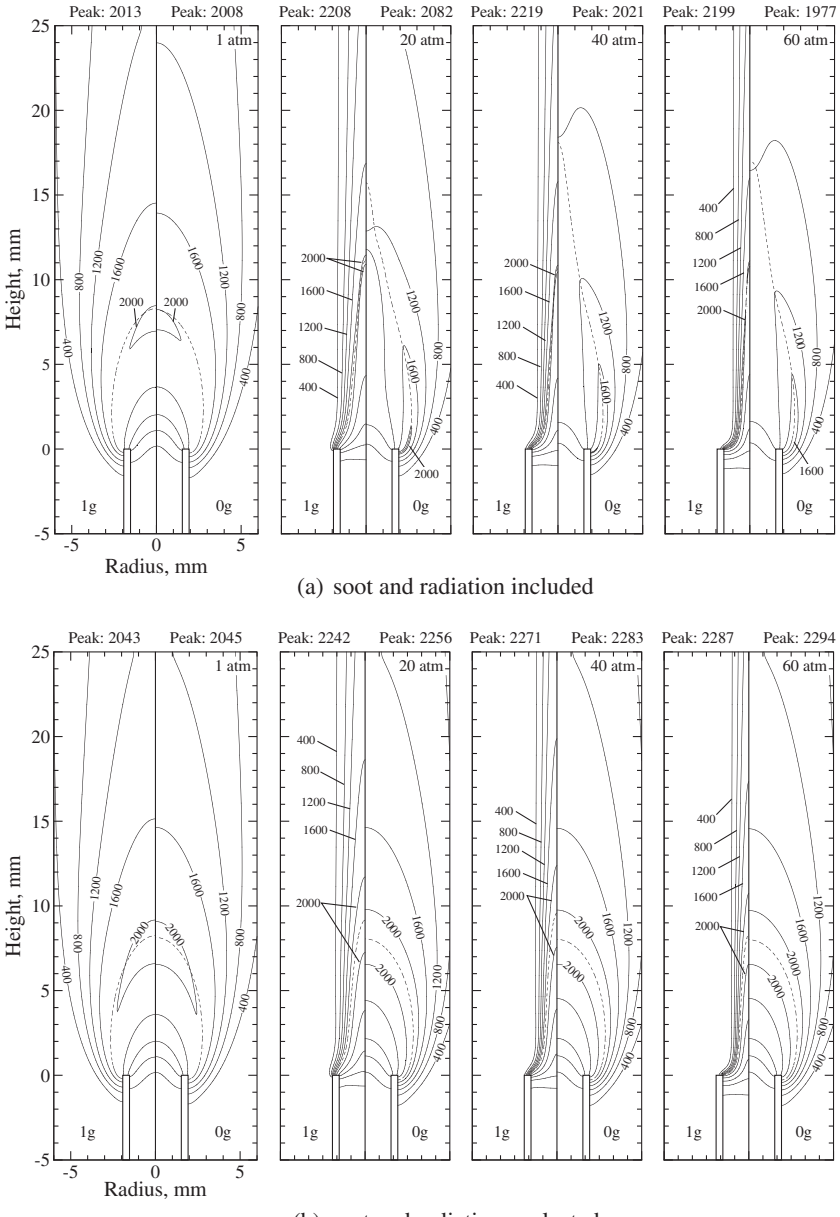

Fig. 9. Predicted temperature contours for the normal-gravity (left) and zero-gravity (right) flames. Units in K. The dashed black lines correspond to the location where the mixture fraction is equal to the stoichiometric value.

The impact of radiation on temperature is confirmed by comparing predictions obtained without soot and radiation, Fig. 9b, to predictions obtained when they are both included, Fig. 9a. Considering the temperature predictions obtained without soot and radiation, peak temperatures steadily increase with pressure, regardless of gravity level. Temperatures are marginally higher in zero-gravity, possibly because the slower velocities provides reactions more time to complete and progress towards equilibrium. When soot and radiation are included, Fig. 9a, peak temperatures of the normal-gravity flames increase with pressure at a slower rate than when they were neglected since any increase in heat-release is counter-acted by radiative heat losses. Radiation effects are much stronger at zero-gravity and, as a result, peak temperatures decrease with increasing pressure when soot and radiation are included. Above 1 atm, the peak temperatures in the zero-gravity flames are significantly lower than those in the normal-gravity flames. These low temperatures in the zero-gravity flames are one of the primary reasons for the decreased sensitivity of η_s to pressure observed above 20 atm.

The divergence of the radiative heat flux, $\nabla \cdot \mathbf{q}_{rad}$, is plotted in Fig. 10 for each flame. Since this quantity varies exponentially over the range of pressures studied, the logarithm of the negative component of $\nabla \cdot \mathbf{q}_{rad}$ is plotted in Fig. 10. At 1 atm, the predicted contours of $\nabla \cdot \mathbf{q}_{rad}$ at normal- and zero-gravity conditions are similar. However, the drastic increase in radiation transport with pressure produces significant differences between the predictions for $\nabla \cdot \mathbf{q}_{rad}$ in the two 60 atm flames. The magnitude of $\nabla \cdot \mathbf{q}_{rad}$ is always slightly larger in the normal-gravity flames, which is a direct result of the steeper temperature and soot concentration gradients in the normal-gravity flames at high pressures. However, radiation has a stronger impact in zero-gravity since velocities are lower. There is also a significant amount of energy transported upstream into the coflow-air supply tube. While this upstream energy transport vanishes under normal-gravity conditions when pressure is increased to 60 atm, it intensifies with pressure in the absence of gravity.

5.4. Species mass fractions

In the presence of gravity, buoyant forces rapidly accelerate the flow upward. The accelerating flow entrains the surrounding coflowing oxidizer stream and mixes the oxidizer with fresh fuel. Since buoyancy-induced acceleration scales with p^2g, increasing pressure intensifies entrainment and speeds up oxidative pyrolysis. This phenomenon is observed in Fig. 11a, which shows the predicted contours of methane mass fraction in the normal- and zero-gravity flames. At normal-gravity, methane is consumed at a faster rate as pressure is increased from 1 to 60 atm. Early fuel pyrolysis is also observed inside the fuel tube at high pressures. This is possibly a result of high temperatures near the tube wall which result from the adiabatic boundary conditions. When gravity is eliminated, increasing pressure while maintaining fixed mass flow rates has the opposite effect since flow velocities are reduced. As such, convective transport slows and fuel consumption rates decrease. The lower temperatures at high pressure also contribute to the observed delay in fuel consumption. Additionally, longer residence times as pressure is increased in zero-gravity may allow axial diffusion to drive fuel downstream. Some early fuel pyrolysis is observed in zero-gravity due to the high temperatures near the wall, which is depicted in Fig. 9a.

When soot and radiation are neglected, there is not much change in the normal-gravity results for methane mass fraction, Fig. 11b. However, the delayed fuel consumption with increasing pressure in zero-gravity, observed in Fig. 11a, does not occur. This is because temperatures are much higher when soot and radiation are neglected.

Regardless of gravity level, acetylene mass fractions decrease with increasing pressure, Fig. 12a. This decrease is partially attributed to the consumption of acetylene through Reactions (R1) and (R2) to produce soot. In both cases, normal- and zero-gravity, acetylene is formed downstream of the fuel tube and peaks along the centerline at 1 atm. However, the peak in all flames above 1 atm occurs further upstream in an annular region near the fuel tube wall where temperatures are high (see Fig. 9a). It is at these higher pressures where the main differences occur between flames at the two gravity levels. For instance, acetylene completely disappears along the centerline of the zero-gravity flames above 10 atm. This is attributed to the decrease in temperature along the centerline which results as pressure is increased in the absence of gravity. In the normal-gravity flames, a considerable amount of acetylene is observed inside the fuel tube. Acetylene first appears inside the tube at 10 atm and concentrations increase when pressure is raised to 20 atm. However, acetylene concentrations begin to decrease with further increases in pressure. This behavior results from the competition between several processes which intensify at higher pressures: (1) acetylene production inside the tube due to fuel preheating, and (2) consumption of acetylene to produce soot.This competition is confirmed by comparing the predictions

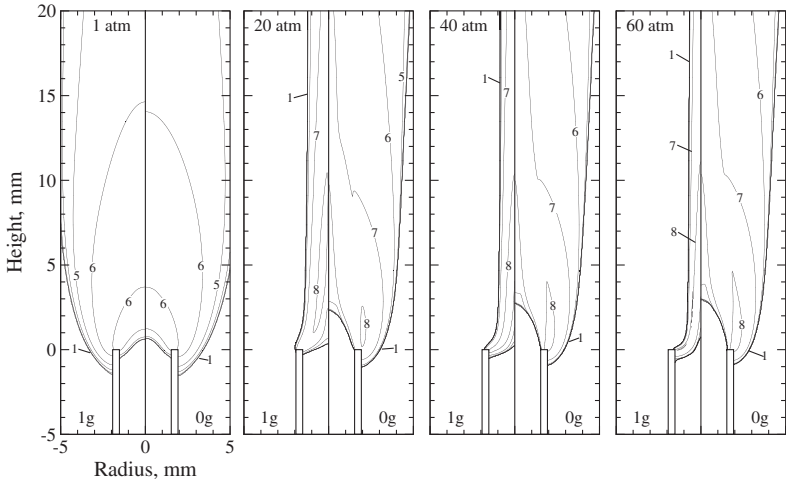

Fig. 10. Predicted contours of the divergence of the radiative heat flux, $\nabla \cdot \mathbf{q}_{rad}$. Contours correspond to $\log_{10}[\max(-\nabla \cdot \mathbf{q}_{rad}), 1]$.

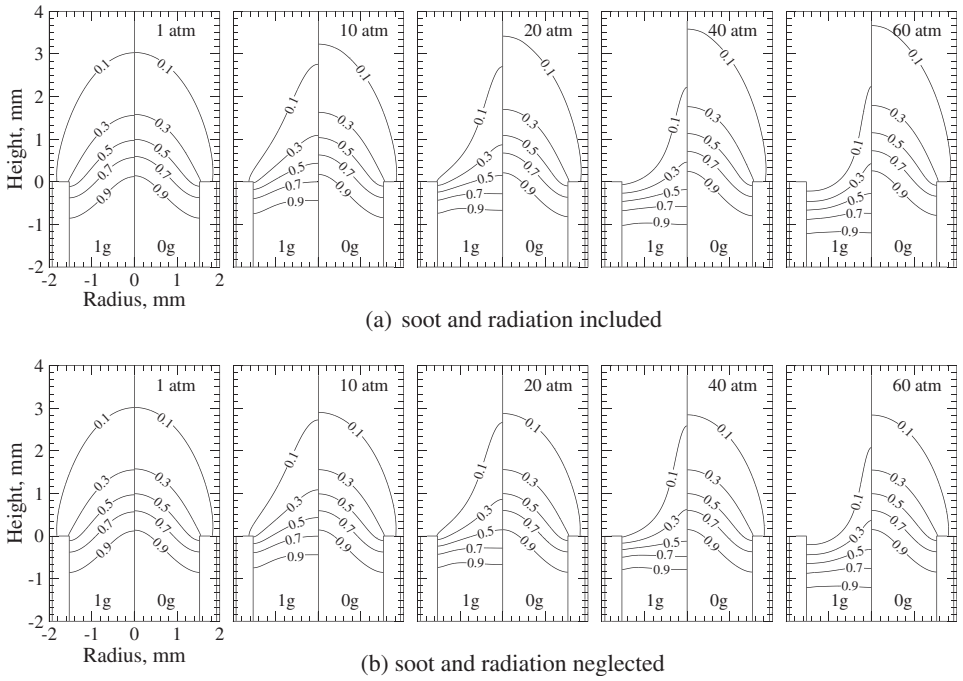

Fig. 11. Predicted contours for methane mass fraction in the normal-gravity (left) and zero-gravity (right) flames.

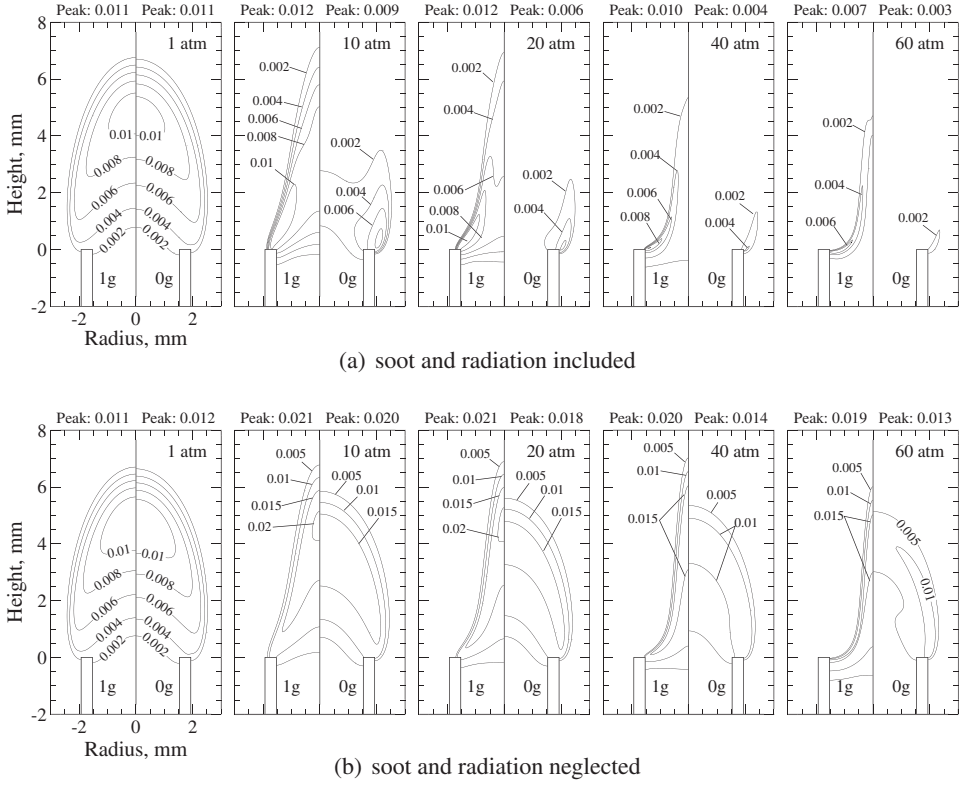

Fig. 12. Predicted contours for acetylene mass fraction in the normal-gravity (left) and zero-gravity (right) flames.

obtained with and without soot and radiation, Fig. 12a and b. When soot and radiation are neglected, acetylene concentrations inside the fuel tube of the normal-gravity flames increase steadily with pressure. Here, the effects of fuel preheating are still present but there is no gas-to-soot conversion to consume acetylene.

Several factors contribute to the higher acetylene concentrations observed under normal-gravity conditions.

(1) The longer residence times in the zero-gravity flames promote the conversion of acetylene to soot.
(2) Temperatures inside the fuel tube and near the wall are higher at normal-gravity because radiation has less impact and buoyant forces contract the flame towards the centerline. These higher temperatures promote the breakdown of fuel and the production of acetylene.

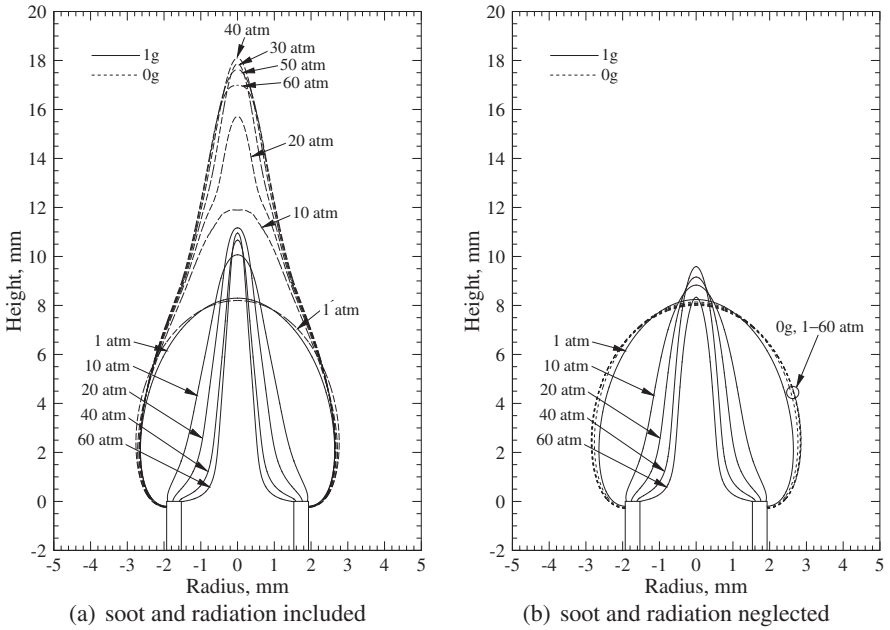

Fig. 13. The effect of pressure and gravity on the stoichiometric mixture fraction surface.

(3) Entrainment of air into the flame base, which also promotes fuel pyrolysis, intensifies with pressure at normal-gravity while it does not change much with pressure at zero-gravity.

These last two items are confirmed by comparing predictions obtained with and without soot and radiation, Fig. 12a and b. Neglecting soot and radiation, peak acetylene concentrations are almost constant between 10 and 60 atm at normal-gravity. However, they decrease significantly with pressure for zero-gravity. The large initial increase in acetylene production between 1 and 10 atm for both normal- and zero-gravity flames occurs because of the ten-fold increase in pressure.

5.5. Flame geometry

Since the zero-gravity flames begin smoking at relatively low pressures—that is, below 20 atm—it is difficult to compare the visible flame geometry. Typically, the predicted visible flame shape would be defined as the location where the soot volume fraction is equal to a certain value. Instead, we focus on the flame shape defined by the stoichiometric mixture fraction (22) and (22).

The shapes of the normal- and zero-gravity flames, illustrated in Fig. 13a, are similar at 1 atm where the effects of buoyancy are small. However, above this pressure, the zero-gravity flames become significantly longer and wider than the normal-gravity flames. Flame width decreases with increasing pressure at normal-gravity in accordance with previous findings [17–21], but remains roughly unchanged with pressure at zero-gravity. This narrowing of the normal-gravity flames occurs because, as pressure is increased, buoyant forces contract streamlines inwards. Pressure has virtually no effect on the path of the streamlines in zero-gravity; it only effects the magnitudes of velocities throughout the flame.

The height of the normal-gravity flames increases significantly from 1 to 20 atm, but remains roughly constant with any further increases in pressure. It is not clear what causes this increase in height since the flames are all buoyancy-controlled (Froude number $\ll 1$) within the range of pressures studied. A much larger increase in height is observed as pressure is increased in zero-gravity due to the higher soot concentrations and large decrease in temperature. This is confirmed by comparing the results obtained with and without the inclusion of soot and radiation effects, Fig. 13a and b. Without soot and radiation, the zero-gravity flames are much shorter and their shape is completely independent of pressure. The length of the non-sooting flames is also shorter when gravity is absent. This suggests that diffusion times are large enough that combustion is not hindered by slowing velocities and reduced convective transport.

6. Concluding remarks

The methane laminar coflow diffusion flames of Joo and Gülder [20] were studied numerically to assess the predictive capabilities of a simple, acetylene-based soot model and help explain a number of the experimental findings. Calculations were also performed without gravity to isolate the effects of buoyancy and pressure on sooting characteristics and flame structure. Pressures considered ranged from 1 to 60 atm.

In order to obtain converged, steady-state solutions for the high pressure (30–60 atm) normal-gravity flames, modifications to the soot model were required which included assuming a constant number density. Assuming a fixed number density did not significantly affect the numerical solutions, nor did varying the assumed value of N_s. These results suggest that soot formation is fairly insensitive to nucleation for heavily-sooting flames and that surface growth determines the overall soot mass produced.

Although large discrepancies were observed between the predicted and measured values, the soot model employed in this study was able to predict the overall features and the correct trends with pressure. The soot model predicted the appearance of soot lower in the flame than measured and that soot is formed inside the fuel tube above 10 atm. As a result, the soot concentrations and the visible flame lengths were over-predicted. These discrepancies were attributed to the soot model and uncertainties in the wall boundary conditions. Both temperature and soot volume fraction were over-predicted, which suggests that the adiabatic wall boundary condition over-predicts the temperature of the tube wall. However, it is unclear whether the formation of soot inside the tube is an artifact of the over-predicted wall temperatures. There is some

experimental evidence to support these high soot concentrations predicted within the fuel tube near the exit [99].

Based on the numerical results, pressure and gravity were observed to significantly influence the sooting behavior and flame structure of laminar diffusion flames. The zero-gravity flames have lower gas temperatures, thicker soot-containing regions and higher soot volume fractions than normal-gravity flames at the same pressure. These differences were negligible at 1 atm, but became larger as pressure was increased. Flames at both levels of gravity displayed a similar power-law relationship between the maximum carbon conversion factor and pressure that weakened as pressure was increased. However, an inverse relationship between pressure and the maximum carbon conversion factor was predicted above 20 atm when gravity was neglected. An investigation of the numerical results has revealed that these differences in the soot-pressure dependence is a result of several factors. At low pressures, the predicted temperatures and acetylene mass fractions for flames at the two gravity levels are similar because soot volume fractions are low and the effects of buoyancy are minimized. However, residence times become long and soot volume fractions high as pressure is increased above 20 atm in zero-gravity, promoting large radiation losses and reducing temperatures. This decreases soot formation rates in the zero-gravity flames and causes the carbon conversion factor to decrease as pressure is increased beyond 20 atm. Low acetylene concentrations at high pressures also contribute to this behavior.

Flame shape was observed to change when gravity and pressure were varied. The zero-gravity flames become longer while the normal-gravity flames narrowed when pressure was increased. This lengthening of the zero-gravity flames was attributed to the low temperatures and slow oxidation of soot which results at high pressures. This suspicion was confirmed as it was also shown that all of the flames became shorter when soot and radiation were neglected. In fact, the shape of zero-gravity flames is only affected by soot and radiation.

Future work will include more detailed gas-phase kinetic mechanisms that describe the formation of large molecular weight soot precursors and more realistic models for soot [7,58]. Conjugate heat transfer between the tube wall and surrounding hot gases will also be more thoroughly investigated.

Acknowledgments

We thank Hyun I. Joo for providing assistance with the experimental data. Operational funds for this work have been provided by the Natural Sciences and Engineering Research Council (NSERC) and the Canadian Space Agency (CSA). Computational resources for performing all of the calculations reported herein were provided by the SciNet High Performance Computing Consortium at the University of Toronto and Compute/Calcul Canada through funding from the Canada Foundation for Innovation (CFI) and the Province of Ontario, Canada.

References

[1] I. Glassman, P. Yaccarino, Proc. Combust. Inst. 18 (1981) 1175–1183.
[2] J.H. Kent, H.G. Wagner, Proc. Combust. Inst. 20 (1984) 1007–1015.
[3] R.J. Santoro, T.T. Yeh, J.J. Horvath, H.G. Semerjian, Combust. Sci. Technol. 53 (1987) 89–115.
[4] C.M. Megaridis, R.A. Dobbins, Combust. Sci. Technol. 66 (1989) 1–16.
[5] K.T. Walsh, J. Fielding, M.D. Smooke, M.B. Long, A. Linan, K. Annamalai, V.R. Katta, J. Jeffries, B. Dally, Proc. Combust. Inst. 30 (2005) 357–365.
[6] B.M. Kumfer, S.A. Skeen, R. Chen, R.L. Axelbaum, Combust. Flame 147 (2006) 233–242.
[7] A. D'Anna, J.H. Kent, Combust. Flame 152 (2008) 573–587.
[8] S.B. Dworkin, M.D. Smooke, V. Giovangigli, Proc. Combust. Inst. 32 (2009) 1165–1172.
[9] Q. Zhang, M.J. Thomson, H. Guo, F. Liu, G.J. Smallwood, Combust. Flame 156 (2009) 697–705.
[10] H. Guo, K.A. Thomson, G.J. Smallwood, Combust. Flame 156 (2009) 1135–1142.
[11] R.S. Mehta, D.C. Haworth, M.F. Modest, Proc. Combust. Inst. 32 (2009) 1327–1334.
[12] N. Peters, Proc. Combust. Inst. 21 (1988) 1231–1250.
[13] C.K. Law, G.M. Faeth, Prog. Energy Combust. Sci. 20 (1994) 65–113.
[14] I. Glassman, Proc. Combust. Inst. 27 (1998) 1589–1596.
[15] I.M. Miller, H.G. Maahs, High-Pressure Flame Systems for Pollution Studies with Results for Methane–Air Diffusion Flames, TN D-8407, NASA, 1977.
[16] W.L. Flower, C.T. Bowman, Proc. Combust. Inst. 21 (1988) 1115–1124.
[17] L.L. McCrain, W.L. Roberts, Combust. Flame 140 (2005) 60–69.
[18] K.A. Thomson, Ö.L. Gülder, E.J. Weckman, R.A. Fraser, G.J. Smallwood, D.R. Snelling, Combust. Flame 140 (2005) 222–232.
[19] D.S. Bento, K.A. Thomson, Ö.L. Gülder, Combust. Flame 145 (2006) 765–778.
[20] H.I. Joo, Ö.L. Gülder, Proc. Combust. Inst. 32 (2009) 769–775.
[21] F. Liu, K. Thomson, H. Guo, G.J. Smallwood, Combust. Flame 146 (2006) 456–471.
[22] F.G. Roper, Combust. Flame 29 (1977) 219–226.
[23] F.G. Roper, C. Smith, A.C. Cunningham, Combust. Flame 29 (1977) 227–234.
[24] M.R.J. Charest, H.I. Joo, Ö.L. Gülder, C.P.T. Groth, Proc. Combust. Inst. 33 (2011) 549–557.
[25] W. Lee, Y.D. Na, J. Soc. Mech. Eng. Int. J. Ser. B 43 (2000) 550–555.
[26] T.H. Cochran, Experimental Investigation of Laminar Gas Jet Diffusion Flames in Zero Gravity, Technical Report, NASA-TN-D-6523, 1972.
[27] C.R. Kaplan, E.S. Oran, K. Kailasanath, H.D. Ross, Proc. Combust. Inst. 26 (1996) 1301–1309.
[28] P.B. Sunderland, B.J. Mendelson, Z.G. Yuan, D.L. Urban, Combust. Flame 116 (1999) 376–386.
[29] S.H. Chung, C.K. Law, Combust. Sci. Technol. 37 (1984) 21–46.
[30] M.Y. Bahadori, R.B. Edelman, D.P. Stocker, S.L. Olson, AIAA J. 28 (1990) 236–244.
[31] E. Villermaux, D. Durox, Combust. Sci. Technol. 84 (1992) 279–294.
[32] S.S. Krishnan, J.M. Abshire, P.B. Sunderland, Z.. Yuan, J.P. Gore, Combust. Theory Modell. 12 (2008) 605–620.
[33] P.B. Sunderland, S. Mortazavi, G.M. Faeth, D.L. Urban, Combust. Flame 96 (1994) 97–103.
[34] F.J. Diez, C. Aalburg, P.B. Sunderland, D.L. Urban, Z.G. Yuan, G.M. Faeth, Combust. Flame 156 (2009) 1514–1524.
[35] P.S. Greenberg, Laser doppler velocimetry and full-field soot volume fraction measurements in microgravity, in: Proceedings of the 3rd International Microgravity Combustion Workshop, NASA, Cleveland, OH, 1995, pp. 247–252, 1995.
[36] J.C. Ku, D.W. Griffin, P.S. Greenberg, J. Roma, Combust. Flame 102 (1995) 216–218.
[37] J. Reimann, S. Will, Microgravity Sci. Technol. 15 (2005) 333–337.
[38] D.L. Urban, Z.G. Yuan, P.B. Sunderland, K.C. Lin, Z. Dai, G.M. Faeth, Proc. Combust. Inst. 28 (2000) 1965–1971.
[39] P.B. Sunderland, Ü.Ö. Köylü, G.M. Faeth, Combust. Flame 100 (1995) 310–322.
[40] P.B. Sunderland, G.M. Faeth, Soot Nucleation and Growth in Weakly-bouyant Hydrocarbon Diffusion Flames, Technical Report, AIAA-1995-149, 1995.
[41] P.B. Sunderland, G.M. Faeth, Combust. Flame 105 (1996) 132–146.
[42] N. Panek, Ö.L. Gülder, Simulation of microgravity diffusion flames using sub-atmospheric pressures, in: 48th AIAA Aerospace Sciences Meeting, Orlando, Florida, AIAA 2010-1477, 2010.
[43] P.S. Greenberg, J.C. Ku, Combust. Flame 108 (1997) 227–230.
[44] R.L. Vander Wal, Microgravity Sci. Technol. 10 (1997) 66–74.
[45] K.T. Walsh, J. Fielding, M.D. Smooke, M.B. Long, Proc. Combust. Inst. 28 (2000) 1973–1979.
[46] D.L. Urban, Z.G. Yuan, P.B. Sunderland, G.T. Linteris, J.E. Voss, K.C. Lin, Z. Dai, K. Sun, G.M. Faeth, AIAA J. 36 (1998) 1346–1360.
[47] K.C. Lin, Z. Dai, G.M. Faeth, Laminar soot processes, in: Fifth International Microgravity Combustion Workshop, NASA, Cleveland, OH, 1999, pp. 147–150, 1999.
[48] O.A. Ezekoye, Z. Zhang, Combust. Flame 110 (1997) 127–139.
[49] G. Legros, A. Fuentes, S. Rouvreau, P. Joulain, B. Porterie, J.L. Torero, Proc. Combust. Inst. 32 (2009) 2461–2470.
[50] W. Kong, F. Liu, Combust. Theory Modell. 13 (2009) 993–1023.
[51] W. Kong, F. Liu, Microgravity Sci. Technol. 22 (2010) 205–214.
[52] Z. Zhang, O.A. Ezekoye, Combust. Sci. Technol. 137 (1998) 323–346.
[53] I.M. Kennedy, Prog. Energy Combust. Sci. 23 (1997) 95–132.
[54] K.M. Leung, R.P. Lindstedt, W.P. Jones, Combust. Flame 87 (1991) 289–305.
[55] M. Fairweather, W.P. Jones, R.P. Lindstedt, Combust. Flame 89 (1992) 45–63.
[56] H. Guo, F. Liu, G.J. Smallwood, Ö.L. Gülder, Combust. Flame 145 (2006) 324–338.
[57] M. Frenklach, H. Wang, Springer Ser. Chem. Phys. 59 (1994) 165–192.
[58] J. Appel, H. Bockhorn, M. Frenklach, Combust. Flame 121 (2000) 122–136.
[59] A. D'Anna, G. Mazzotti, J. Kent, Combust. Sci. Technol. 176 (2004) 753–767.
[60] H. Guo, G.J. Smallwood, Combust. Sci. Technol. 180 (2008) 1695–1708.
[61] R.J. Hall, M.D. Smooke, M.B. Colket, in: F.L. Dryer, R.F. Sawyer (Eds.), Physical and Chemical Aspects of Combustion: A Tribute to Irvin Glassman, Gordon & Breach, Amsterdam, 1997, pp. 189–230.
[62] M.D. Smooke, C.S. McEnally, L.D. Pfefferle, R.J. Hall, M.B. Colket, Combust. Flame 117 (1999) 117–139.
[63] Q. Zhang, H. Guo, F. Liu, G.J. Smallwood, M.J. Thomson, Combust. Theory Modell. 12 (2008) 621–641.

[64] Y. Zhang, C. Seigneur, J.H. Seinfeld, M.Z. Jacobson, F.S. Binkowski, Aerosol Sci. Technol. 31 (1999) 487–514.
[65] P.R. Lindstedt, Springer Ser. Chem. Phys. 59 (1994) 417–441.
[66] H. Richter, S. Granata, W.H. Green, J.B. Howard, Proc. Combust. Inst. 30 (2004) 1397–1405.
[67] M.R.J. Charest, C.P.T. Groth, Ö.L. Gülder, Combust. Theory Modell. 14 (2010) 793–825.
[68] K.K. Kuo, Principles of Combustion, second ed., John Wiley & Sons, Inc., New Jersey, 2005.
[69] J.O. Hirschfelder, C.F. Curtiss, R.B. Byrd, Molecular Theory of Gases and Liquids, John Wiley & Sons, New York, 1969.
[70] L. Talbot, R.K. Cheng, R.W. Schefer, D.R. Willis, J. Fluid Mech. 101 (1980) 737–758.
[71] I.M. Kennedy, W. Kollmann, J.Y. Chen, Combust. Flame 81 (1990) 73–85.
[72] A. Gomez, D.E. Rosner, Combust. Sci. Technol. 89 (1993) 335–362.
[73] F. Liu, H. Guo, G.J. Smallwood, Ö.L. Gülder, J. Quant. Spectrosc. Radiat. Transfer 73 (2002) 409–421.
[74] M. Frenklach, Phys. Chem. 4 (2002) 2028–2037.
[75] M.D. Smooke, M.B. Long, B.C. Connelly, M.B. Colket, R.J. Hall, Combust. Flame 143 (2005) 613–628.
[76] J. Nagle, R.F. Strickland-Constable, Oxidation of carbon between 1000–2000 °C, in: Proceedings of the Fifth Conference on Carbon, Pergamon Press, London, 1962, pp. 154–164.
[77] J.B. Moss, C.D. Stewart, K.J. Young, Combust. Flame 101 (1995) 491–500.
[78] D. Bradley, G. Dixon-Lewis, S.E. Habik, E.M.J. Mushi, Proc. Combust. Inst. 20 (1984) 931–940.
[79] B.G. Carlson, K.D. Lathrop, in: H. Greenspan, C.N. Kelber, D. Okrent (Eds.), Computing Methods in Reactor Physics, Gordon and Breach, London, 1968, pp. 171–266.
[80] C.P. Thurgood, A. Pollard, H.A. Becker, J. Heat Transfer 117 (1995) 1068–1070.
[81] F. Liu, G.J. Smallwood, Ö.L. Gülder, J. Thermophys. Heat Transfer 14 (2000) 278–281.
[82] F. Liu, G.J. Smallwood, Ö.L. Gülder, Int. J. Heat Mass Transfer 43 (2000) 3119–3135.
[83] F. Liu, H. Guo, G.J. Smallwood, Combust. Flame 138 (2004) 136–154.
[84] A. Soufiani, J. Taine, Int. J. Heat Mass Transfer 40 (1997) 987–991.
[85] F. Liu, G.J. Smallwood, Ö.L. Gülder, J. Quant. Spectrosc. Radiat. Transfer 68 (2001) 401–417.
[86] V. Goutiere, A. Charette, L. Kiss, Numer. Heat Transfer, Part B 41 (2002) 361–381.
[87] S.A. Northrup, C.P.T. Groth, Solution of laminar combusting flows using a parallel implicit adaptive mesh refinement algorithm, in: Proceedings of the Fourth International Conference on Computational Fluid Dynamics, ICCFD4, Ghent, Belgium, pp. 341–346, 2006.
[88] X. Gao, C.P.T. Groth, Int. J. Comput. Fluid Dyn. 20 (2006) 349–357.
[89] P.L. Roe, J. Comput. Phys. 43 (1981) 357–372.
[90] W.J. Coirier, K.G. Powell, AIAA J. 34 (1996) 938–945.
[91] J.M. Weiss, W.A. Smith, AIAA J. 33 (1995) 2050–2057.
[92] D.G. Goodwin, Chem. Vap. Deposition XVI and EUROCVD 14 (2003) 155–162.
[93] G.P. Smith, D.M. Golden, M. Frenklach, N.W. Moriarty, B. Eiteneer, M. Goldenberg, C.T. Bowman, R.K. Hanson, S. Song, W.C. Gardiner, Jr., V.V. Lissianski, Z. Qin, Gri-mech 3.0, 2002. http://www.me.berkeley.edu/gri_mech/.
[94] H. Guo, F. Liu, G.J. Smallwood, Ö.L. Gülder, Combust. Theory Modell. 6 (2002) 173–187.
[95] Ö.L. Gülder, K.A. Thomson, D.R. Snelling, Combust. Flame 144 (2006) 426–433.
[96] J.H. Kent, H.G. Wagner, Combust. Sci. Technol. 41 (1984) 245–269.
[97] Y.R. Sivathanu, J.P. Gore, Combust. Flame 97 (1994) 161–172.
[98] Y.R. Sivathanu, J.P. Gore, Combust. Flame 110 (1997) 256–263.
[99] P.M. Mandatori, Ö.L. Gülder, Combust. Flame 150 (2007) 400–403.
[100] H.I. Joo, Ö.L. Gülder, Combust. Flame 157 (2010) 408–409.
[101] D.R. Honnery, J.H. Kent, Combust. Flame 82 (1990) 426–434.
[102] J.H. Kent, D.R. Honnery, Combust. Sci. Technol. 75 (1991) 167–177.
[103] R.W. Bilger, Proc. Combust. Inst. 22 (1989) 475–488.